

# Experimental evidence of transition between dynamical and kinematical diffraction regimes in ion-implanted Si observed through X-ray multiple-beam diffraction mappings

Guilherme A. Calligaris, Rossano Lang, Jefferson Bettini, Adenilson O. dos Santos, and Lisandro P. Cardoso

Citation: *Appl. Phys. Lett.* **109**, 141901 (2016); doi: 10.1063/1.4963791

View online: <https://doi.org/10.1063/1.4963791>

View Table of Contents: <http://aip.scitation.org/toc/apl/109/14>

Published by the [American Institute of Physics](#)

---

## Articles you may be interested in

[Millisecond direct measurement of the magnetocaloric effect of a Fe<sub>2</sub>P-based compound by the mirage effect](#)

*Applied Physics Letters* **108**, 012407 (2016); 10.1063/1.4939451

[Realizing in-plane surface diffraction by x-ray multiple-beam diffraction with large incidence angle](#)

*Applied Physics Letters* **105**, 181903 (2014); 10.1063/1.4901046

[Enhancement of carrier lifetimes in type-II quantum dot/quantum well hybrid structures](#)

*Journal of Applied Physics* **120**, 084305 (2016); 10.1063/1.4961534

[Residual stress in nano-structured stainless steel \(AISI 316L\) prompted by Xe<sup>+</sup> ion bombardment at different impinging angles](#)

*Journal of Applied Physics* **120**, 145306 (2016); 10.1063/1.4964429

[The Uhlenbeck-Ford model: Exact virial coefficients and application as a reference system in fluid-phase free-energy calculations](#)

*The Journal of Chemical Physics* **145**, 194101 (2016); 10.1063/1.4967775

---



**THE WORLD'S RESOURCE FOR  
VARIABLE TEMPERATURE  
SOLID STATE CHARACTERIZATION**



OPTICAL STUDIES SYSTEMS



SEEBECK STUDIES SYSTEMS



MICROPROBE STATIONS



HALL EFFECT STUDY SYSTEMS AND MAGNETS

[WWW.MMR-TECH.COM](http://WWW.MMR-TECH.COM)

## Experimental evidence of transition between dynamical and kinematical diffraction regimes in ion-implanted Si observed through X-ray multiple-beam diffraction mappings

Guilherme A. Calligaris,<sup>1</sup> Rossano Lang,<sup>2</sup> Jefferson Bettini,<sup>3</sup> Adenilson O. dos Santos,<sup>4</sup> and Lisandro P. Cardoso<sup>1,a)</sup>

<sup>1</sup>*Institute of Physics Gleb Wataghin—IFGW, University of Campinas—UNICAMP, Campinas SP 13083-859, Brazil*

<sup>2</sup>*Institute of Science and Technology—ICT, Federal University of São Paulo—UNIFESP, São José dos Campos SP 12231-280, Brazil*

<sup>3</sup>*Brazilian Nanotechnology National Laboratory—LNNano, Campinas SP 13083-970, Brazil*

<sup>4</sup>*CCSST, Federal University of Maranhão—UFMA, Imperatriz MA 65900-410, Brazil*

(Received 14 May 2016; accepted 18 September 2016; published online 3 October 2016)

In this paper, the dependence of a Laue diffraction streak on the crystalline perfection of Xe-implanted Si(001) substrates is presented, based on the observation in the X-ray multiple diffraction (XRMD) mappings, as an experimental evidence of the transition between dynamical and kinematical diffraction regimes. A direct observation of the implanted region by transmission electron microscopy revealed an amorphous Si layer, which recrystallizes into a heavily twinned and faulted microstructure after thermal treatment at 800 °C. Besides the lattice damages, the annealing induces the formation of Xe bubbles. Both singularly affect the XRMD pattern, primarily the four-fold streaks profile of the (000)(002)(1 $\bar{1}\bar{1}$ )(1 $\bar{1}\bar{3}$ ) four-beam simultaneous case when compared with the pristine Si pattern, highlighting the intra- and inter-block diffractions and the role played by the primary extinction effect. Such features provide information on the dominant diffraction regime. The findings are also discussed and compared to the conventional reciprocal space mappings via the asymmetric Si(113) reflection. *Published by AIP Publishing.*

[<http://dx.doi.org/10.1063/1.4963791>]

The possibility of observing a physical phenomenon usually arises from a new approach or from the sensitivity improvement of a technique for material analysis, as in the case of the X-ray multiple diffraction (XRMD).<sup>1,2</sup> Among its most important applications as a fine probe to study crystalline materials, stands out interesting complementary contributions in semiconducting systems that include epitaxial structures, interfaces and surfaces.<sup>3–9</sup> Here, the lattice of an epitaxial layer or an ion implanted region together with the substrate can be investigated separately just by selecting one appropriate reflection peak.

An XRMD occurs when an incident beam simultaneously satisfies the Bragg's law for more than one set of lattice planes within a single crystal. Primary Bragg lattice planes ( $h_p, k_p, l_p$ ) are adjusted ( $\omega$  angle) to diffract the incident beam. By rotating the sample ( $\phi$  azimuthal angle) around the primary reciprocal lattice vector, generally normal to the surface, without losing the Bragg primary reflection intensity, several secondary planes ( $h_s, k_s, l_s$ ) within the single crystal with an arbitrary orientation regarding the surface are also brought into diffraction condition for the same incident beam. The interference among the diffracted beams modifies the primary intensity profile that can be monitored and acquired by a Renninger scan ( $I_{\text{primary}}$  versus  $\phi$  angle).<sup>10</sup> Further details can be found in Ref. 9.

When a set of primary and secondary reflections is chosen, the diffraction regime (dynamical, kinematical or

mixed) will depend on the dimension of the perfect region in the crystal block that is parallel to the crystal surface.<sup>11</sup> Under dynamical (kinematical) diffraction, the transfer of momentum to the surface obeys a primary (secondary) extinction process. If the crystal is ideally imperfect, i.e., with small perfect diffracting regions (understood here as a mosaic crystal), an inter-block diffraction takes place and the kinematical diffraction governs this process. On the other hand, when the crystal perfect regions become large enough (such as in a quasi-perfect crystal) and allow intra-block scattering, the dynamical diffraction regime dominates. The transition between such regimes has already been addressed for the two-beam conventional diffraction case.<sup>12,13</sup>

In this paper, we report an experimental evidence of the transition between dynamical and kinematical regimes in ion-implanted Si samples, inferred through detailed analyses of XRMD mappings of the (000)(002)(1 $\bar{1}\bar{1}$ )(1 $\bar{1}\bar{3}$ ) four-beam simultaneous case. The mappings show an interesting dependence of the (1 $\bar{1}\bar{1}$ ) Laue diffraction streak on the crystalline perfection of the analyzed Si region: streak suppression (for quasi-perfect crystal—primary extinction process) and emergence (for mosaic crystal—secondary extinction process). The results are also discussed and compared to reciprocal space mappings (RSM) via the (113) asymmetric Si reflection. For a support, the crystalline perfection was accessed by transmission electron microscopy (TEM). However, this work is not only limited to the experimental measurements, but the attenuation depth of the incident X-ray beams, considering the  $hkl$  reflections used in the experiments, has also been evaluated.

<sup>a)</sup> Author to whom correspondence should be addressed. Electronic mail: [cardoso@ifi.unicamp.br](mailto:cardoso@ifi.unicamp.br)

The system under study comprises an n-type Czochralski Si(001) wafer (thickness 500  $\mu\text{m}$ ) implanted with  $\text{Xe}^+$  ions with an energy of 80 keV at the room temperature with a fluence of  $5 \times 10^{15} \text{ cm}^{-2}$  (projected range of ions  $R_p \approx 45 \text{ nm}$  and  $\Delta R_p \approx 13 \text{ nm}$  according to the SRIM (Stopping and Range of Ions in Matter) calculations).<sup>14</sup> This ion dose is well below the saturation level of  $2 \times 10^{16} \text{ Xe atoms cm}^{-2}$ .<sup>15</sup> Due to the ion-beam energy and temperature of the process, the surface layer has been converted into amorphous Si. A cleaved piece placed in a quartz capsule unsealed was thermally treated at 800 °C for 30 min in air atmosphere. The formation of a thin  $\text{SiO}_2$  layer on the Si surface by thermal oxidation during the annealing is expected and could reduce considerably the Xenon diffusion out the sample.<sup>16</sup>

As starting analysis, the conventional measurements of (113) asymmetric reciprocal space mappings (RSM) were performed on a PANalytical X'Pert PRO MRD triple-axis diffractometer using the  $\text{Cu-K}\alpha 1$  (1.5406 Å) radiation. The Si(113) reflection was chosen in order to obtain near-surface diffracted intensity contributions, since it has a low incident beam angle with respect to the sample surface ( $\omega = 2.82^\circ$ ) and provides both in-plane and out-of-plane useful crystallographic information. The RSM results are shown in Fig. 1, where the plot axes correspond to [001] and [110] directions, i.e.,  $Q_z$  and  $Q_x$ , respectively. Fig. 1(a), RSM from reference pristine Si, exhibits a symmetric and smooth crystal truncation rod (CTR) streak along the  $Q_z$  direction reflecting a good substrate crystal quality. In contrast, the as-implanted sample mapping, as depicted in Fig. 1(b), shows an asymmetric CTR intensity streak that is shifted for lower  $Q_z$  reciprocal space units. Besides the amorphization, the  $\text{Xe}^+$  implantation produces a stress/strain gradient along the ion-beam direction (out-of-plane, the  $Q_z$  direction) underlying the crystal-amorphous (c-a) interface: the region known as “end-of-range of ions.”

Fig. 1(c) shows the recrystallization effect after annealing process at a temperature higher than the silicon solid-phase epitaxy temperature ( $\approx 420^\circ\text{C}$ ). The comparison between the patterns allows observing the same  $Q_z$  contributions from the pristine Si CTR streak (Fig. 1(a)), indicating an effective implanted layer regrowth. However, under a closer inspection, the CTR streak seems to be discontinued

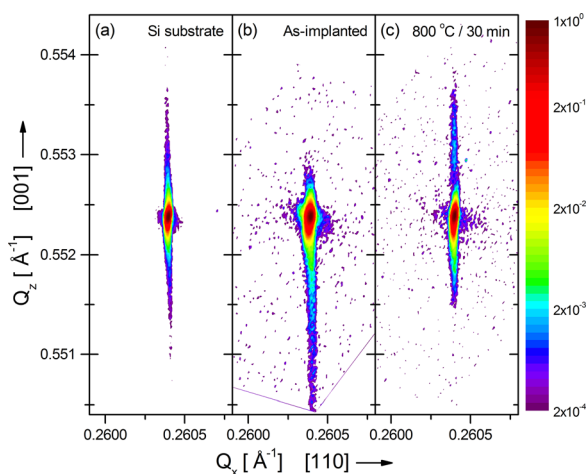


FIG. 1. (113) asymmetric RSM patterns of the samples: (a) pristine Si, (b) as-implanted, and (c) annealed at 800 °C for 30 min.

around the  $0.553 \text{ \AA}^{-1}$ . Furthermore, the  $Q_x$  direction reveals a lateral diffuse scattering due to the high density of the remaining structural defects, such as Si vacancies, and other types of lattice disorder: twins, stacking faults, dislocation loops and  $\{311\}$ 's after the recrystallization at 800 °C. For a review of extended defects induced by ion implantation and annealing, see Ref. 17.

The high resolution Q-scans along the out-of-plane direction in Fig. 2 demonstrate a detailed view of the brief previously discussed effects. The as-implanted sample intensity profile appears broader to lower  $Q_z$  values (positive strain gradient attributed to the presence of self-interstitials) when compared with the pristine Si pattern and has an abrupt drop to the right of the (113) reflection peak (assigned to the accumulation of damage adjacent to the c-a interface).<sup>18</sup> It is well known that the ion implantation process creates an excess of point defects resulting from the atomic collisions. Nevertheless, the annealed sample presents a well-defined region at  $\approx 0.553 \text{ \AA}^{-1}$ , indicating a smaller perpendicular lattice parameter  $a_\perp = 5.425(2) \text{ \AA}$  (compressive strain) when compared with that of the matrix ( $a_{\text{Si}} = 5.431 \text{ \AA}$ ).

Transmission electron microscopy (TEM) was employed as a standard tool for direct observation of the  $\text{Xe}^+$ -implanted region and its structural evolution with temperature. Fig. 3 shows representative cross-sectional TEM images taken at the  $[110]_{\text{Si}}$  zone axis by JEOL JEM-2100F operating at 200 kV. Fig. 3(a) is a sub-surface region image of the as-implanted sample, where one observes an  $\approx 110 \text{ nm}$ -thick amorphous Si-Xe layer produced by the implantation and its respective c-a interface characterized by the clusters of interstitial defects. Selected-area electron diffraction (SAED) patterns (Figs. 3(b) and 3(c)) confirm the amorphous Si-Xe feature, as well as the crystalline Si one. After annealing, the amorphous layer did not recrystallize into a single crystal structure but into a heavily twinned and faulted microstructure. Fig. 3(d) depicts a general overview of the annealed sample, where an  $\approx 18 \text{ nm}$ -thick layer of  $\text{SiO}_2$  is observed at the top of the substrate and lattice damages in two distinct in-depth regions: (i) an array of dislocation loops at  $\approx 115 \text{ nm}$  depth, also called the end-of-range defects that thermally evolved from the clusters of interstitial defects;<sup>19</sup> and (ii) a defect-rich region (extending up to

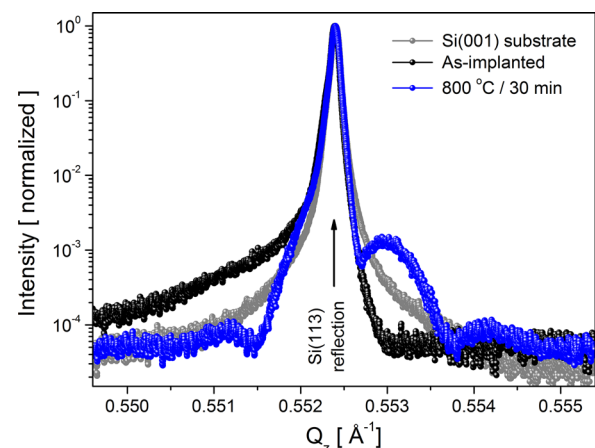


FIG. 2. High resolution Q-scans patterns along the out-of-plane direction for the samples: (a) pristine Si, (b) as-implanted, and (c) annealed.

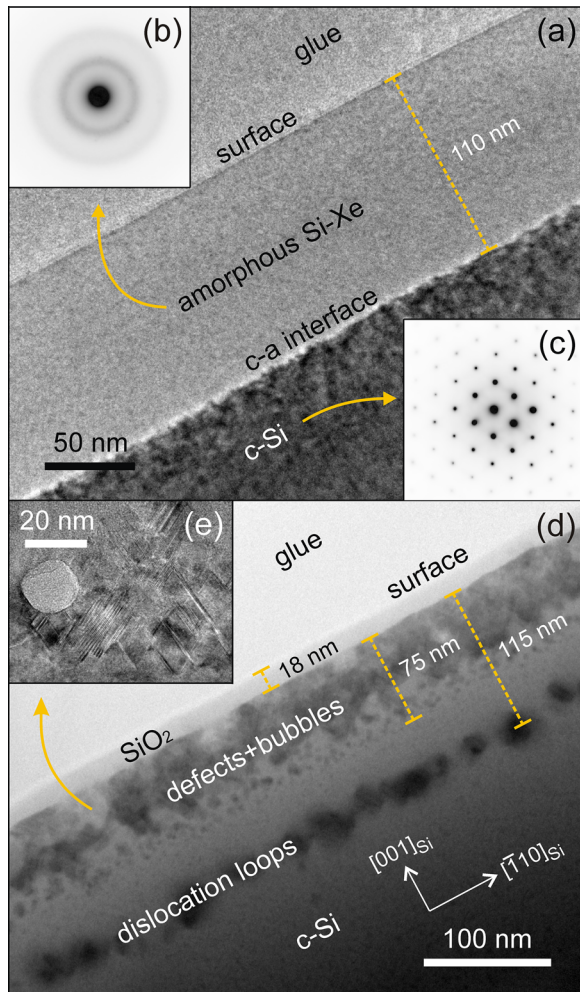


FIG. 3. (a) Cross-sectional TEM image of the as-implanted sample showing an amorphous Si-Xe layer and its respective crystal-amorphous interface. SAED patterns confirming (b) amorphous and (c) crystalline features. (d) Overview of the annealed sample revealing two distinct defects regions at different depths. (e) HRTEM image showing a Xe-bubble surrounded by extended defects.

75 nm depth), consisting of other extended defects (such as  $\{311\}$ 's or “rod-like” defects and Si twins) and embedded Xe nanosized bubbles (ranging from 5 to 20 nm in diameter—Fig. 3(e)).

Mappings of the exact multiple diffraction condition provide information on the crystalline perfection and also allow the identification of the diffraction regime (dynamical, kinematical, or mixed).<sup>11</sup> In this approach, the multiple diffraction angular condition is scanned by varying in a coupled way both  $\omega$  (incidence) and  $\phi$  (azimuthal) angles. Through the analysis of the iso-intensity contours of these  $\omega:\phi$  scan plots, one can obtain the XRMD peak profile and specific details on the lattice coherence along the beam path and, hence, on the crystalline quality. Such mappings were performed at the Brazilian Synchrotron Radiation Facility—LNLS using the  $(000)(002)(1\bar{1}\bar{1})(1\bar{1}\bar{3})$  four-beam simultaneous case. It involves the following reflections: incident  $(000)$ , primary  $(002)$ , first secondary  $(1\bar{1}\bar{1})$  (transmitted case—Laue) and second secondary  $(1\bar{1}\bar{3})$  (reflected case—Bragg). Since  $(002)$  and  $(1\bar{1}\bar{3})$  are Bragg and  $(1\bar{1}\bar{1})$  is Laue transmission reflections, the reflected beams from  $(002)$  and  $(1\bar{1}\bar{3})$  can be observed from a quasi-perfect crystal in the

$\omega:\phi$  mapping. The  $(1\bar{1}\bar{1})$  transmission, however, cannot be seen due to crystal absorption of the transmission geometry. However, if the crystal or a crystal region is imperfect (contains a high density of defects), the scattering streak along the  $(1\bar{1}\bar{1})$  direction can be detected. For such a study, the samples are first aligned for the  $(002)$  reflection and then the  $\omega:\phi$  scans are performed in the vicinity of the four-beam reflection. The incident synchrotron beam energy was 7.98 keV, and no slits or analyzer crystals were introduced into the diffracted beam path towards the detector.

The  $\omega:\phi$  mappings (centered in the XRMD diffraction peak) for the Si substrate, as-implanted and annealed samples are shown in Fig. 4. In the pristine Si mapping exhibited in Fig. 4(a), the main features for perfect or nearly perfect crystals can be observed: symmetric streak and a well-defined XRMD peak—typical of diffraction under dynamical regime, i.e., when primary extinction is the dominant process. On the other hand, the as-implanted sample mapping in Fig. 4(b) clearly shows an asymmetry in the intensity of this streak, a behavior similar to that found in the CTR streak (Fig. 1(b)). A deformation and peak broadening of the exact XRMD condition for the  $\omega$  angle in comparison to the pristine Si, which reflects a small reduction of the lattice coherence length (perfect diffracting block dimension) along the out-of-plane, i.e., the direction ( $\omega$ ), is also evident. However, the mapping for the annealed sample in Fig. 4(c) shows a recovery of the intensity symmetry streak and an additional remarkable streak. Furthermore, a diffuse intensity appears smeared out from the exact XRMD condition.

When indexed, each streak represents a secondary plane that satisfies the diffraction condition along with the primary plane  $(002)$ . This statement is better understood by the illustration in Fig. 4(d), thus showing all the scattering vectors ( $H_P$ —primary and  $H_S$ —secondary) taking part of this XRMD case. Each scattering vector has its own diffracting-cone that characterizes the angular aperture between incident and diffracted beams for the corresponding planes. The point where the cones intercept each other represents the angular position, for which the diffraction condition is satisfied for all the planes and by definition is the XRMD peak position. Therefore, the observed streaks in the mapping area stand for the intensity contribution from the diffraction-cones of each plane involved: primary plane [ $H_P(002)$ ] and two secondary planes [ $H_S(1\bar{1}\bar{1})$  and  $H_S(1\bar{1}\bar{3})$ ].

The mapping in Fig. 4(c) is an example of superimposed XRMD profiles arising from a mixed regime: overlap between the dynamical (scattering within perfect regions—Si bulk) and kinematical (scattering among damaged Si regions) diffraction regimes. According to the TEM observation, the annealed sample has a complex structure that involves several regions with different crystalline perfection. The morphology near the surface encompasses a  $\text{SiO}_2$  thin film, a defective region (consisting of  $\{311\}$  defects, Si twins and Xe nanobubbles), a damage “free” recrystallized region, an array of dislocation loops and, then, Si bulk. Apart from  $\text{SiO}_2$  amorphous,  $\{311\}$ 's, twins and dislocation loops have orientational relationship with the matrix. Some bubbles also present faceted sphere-like shapes. Therefore, the conformations of these defects and bubbles provide the mosaic structure of an ideally imperfect crystal. The kinematical regime

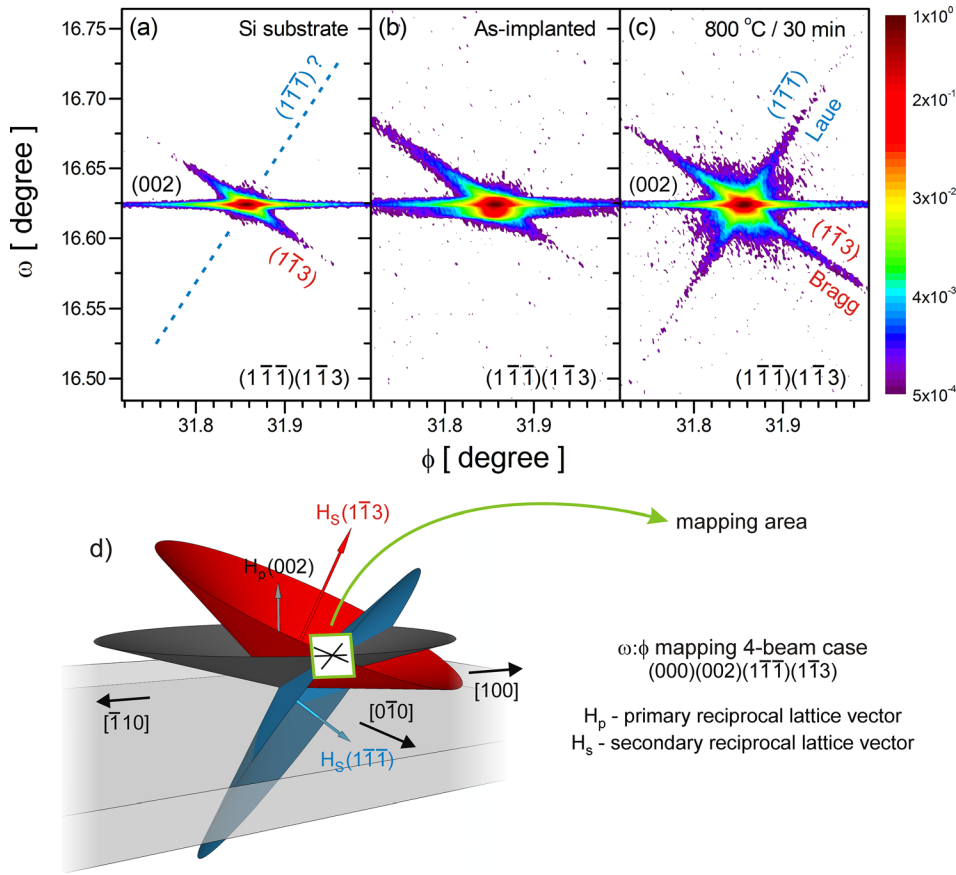


FIG. 4.  $\omega:\phi$  mappings of the (000)(002)(111)(113) four-beam simultaneous case for the samples: (a) pristine Si, (b) as-implanted, and (c) annealed. (d) Diffracting-cone scheme that characterizes the angular aperture between incident and diffracted beams for the following planes: (002) primary and the (111) and (113) secondary ones.

arises significantly as a consequence of the high density of these structural imperfections after the recrystallization process. These defects reduce the dimensions of coherently scattering regions, increase the in-plane mosaic spread and enable the secondary extinction regime given rise to the emergence of the (111) streak. Hence, the (111) streak intensity, that is a Laue transmission, has been suppressed from the Si substrate (pristine) pattern because of the crystal perfection. Therefore, it suffers from primary extinction that causes intensity loss of the diffracted beams.<sup>20</sup> In the as-implanted sample mapping, in Fig. 4(b), the Laue streak is also absent due to the sample microstructure: the amorphous layer at the subsurface (not contributing for diffraction), the strained region near the c-a interface that only causes peak broadening in the  $\omega$  direction, and the crystalline Si (bulk) that effectively contributes to the diffracted intensity. For this sample the positive strain inferred from the RSM/Q-scan seems not breaking the orientation of the diffracting blocks; only elongated them in the  $Q_z$  direction. As a result, the intra-block diffraction still occurs, the dynamical regime persists and the appearance of the (111) streak is inhibited.

Indeed, both Figs. 1 and 4 show the striking results. Nevertheless, one important question still arises: are the intensity contributions detected from the same material region by both techniques RSM/Q-scans and XRMD? In order to address this question, we have evaluated the average penetration depth of an X-ray beam. The attenuation depth can be given by the following expression:<sup>21</sup>

$$\Lambda_{hkl}(\lambda) = \frac{v_c}{4r_0 d_{hkl} |F_{hkl}|}. \quad (1)$$

It represents the beam penetration normal to the sample surface that causes an intensity reduction of  $1/e$  ratio in the incident beam during a symmetric diffraction condition and is usually called as “extinction depth.” Here,  $v_c$  is the Si unit cell volume,  $r_0$  the classic electron radius, and  $d_{hkl}$  and  $|F_{hkl}|$  are the distance and structure factor of the corresponding  $hkl$  reflection, respectively. A necessary geometric correction was considered in order to deal with the asymmetric reflection employed. For the XRMD case, where more than one secondary reflection is under diffraction simultaneously with the incident beam and the primary reflection, an attenuation length  $z_{hkl}$  was derived from  $\Lambda_{hkl}$  (Eq. (1)) and that satisfies the same  $1/e$  attenuation criteria in the usual exponential decay form and can be given by the following expression:

$$I = I_0 \exp[-\mu_{hkl} z_{hkl}] = \frac{I_0}{e}. \quad (2)$$

This defines an attenuation coefficient  $\mu_{hkl}$  for each involved  $hkl$  reflection, which was then used to weight the attenuation caused in the incident beam for each XRMD reflection. This approach was carried out to express the result in terms of depth with respect to the surface. A similar method has been used by Freitas *et al.*<sup>22</sup> The estimated values for the asymmetric (113) reflection RSM/Q-scans and the XRMD four-beam case are  $\Lambda_{(113)}^{RSM} = 190$  nm and  $\Lambda_{(111)(113)}^{XRMD} = 484$  nm, respectively. These values indicate that both techniques probe the same cross-section of the sample near the surface (overlap of the implanted region and a portion of the Si bulk). The reason for the difference between the mapping

results arises from the fact that only XRMD technique has enough sensitivity to discriminate sequential reflections coming from different planes along the scattering path, i.e., capability to distinguish dynamic effects.<sup>23</sup> Therefore, the appearance of the  $(1\bar{1}\bar{1})$  streak in the annealed sample mapping, as depicted in Fig. 4(c), comes from the suppression of the primary extinction effect due to structural imperfections within the “implanted + annealed” layer. In this scenario, the mosaic block dimension is small enough to no longer permit the dynamical coupling between diffracting planes inside the same mosaic block, which breaks the coherence of the diffracted beams. This lack of coherence increases the kinematical-like behavior, since the coupling between diffracting planes is now conducted by distinct mosaic blocks and the diffracted intensity is governed by the secondary extinction.

In sum, lattice damages as well as noble gas bubbles have singularly affected the  $\omega:\phi$  mapping patterns of the exact multiple diffraction condition, even if the analyzed region is near to the surface and has nanometric thickness. The detection of the mixed diffraction regime demonstrates the high sensitivity of the XRMD technique in contrast to the conventional ones. It presents a great advantage over other surface-sensitive techniques, such as grazing-incidence diffraction, which can suffer low diffraction efficiency (due to X-ray total external reflection) and low angular resolution (broad diffuse grazing diffraction peaks).<sup>2</sup>

The authors would like to thank the financial support of the Brazilian agencies CNPq, FAPESP, FAPEMA, the LNLS (XRD2 beamline) staff and Sérgio Morelhão for useful discussions.

- <sup>1</sup>S.-L. Chang, *X-Rays Multiple-Wave Diffraction: Theory and Application* (Springer Verlag, New York, 2004).
- <sup>2</sup>X.-R. Huang, R.-W. Peng, T. Gog, D. P. Siddons, and L. Assoufid, *Appl. Phys. Lett.* **105**, 181903 (2014).
- <sup>3</sup>S. L. Morelhão, L. P. Cardoso, J. M. Sasaki, and M. M. G. Carvalho, *J. Appl. Phys.* **70**, 2589 (1991).
- <sup>4</sup>S. L. Morelhão and L. P. Cardoso, *Solid State Commun.* **88**, 465 (1993).
- <sup>5</sup>M. A. Hayashi, L. H. Avanci, L. P. Cardoso, J. M. Sasaki, L. C. Kretly, and S.-L. Chang, *Appl. Phys. Lett.* **71**, 2614 (1997).
- <sup>6</sup>R. V. Orloski, M. A. A. Pudenzi, M. A. Hayashi, J. W. Swart, and L. P. Cardoso, *J. Mol. Catal. A: Chem.* **228**, 177 (2005).
- <sup>7</sup>W. C. Sun, H. C. Chang, B. K. Wu, Y. R. Chen, C. H. Chu, S.-L. Chang, M. Hong, M. T. Tang, and Y. P. Stetsko, *Appl. Phys. Lett.* **89**, 091915 (2006).
- <sup>8</sup>A. S. de Menezes, A. O. dos Santos, J. M. A. Almeida, J. R. R. Bortoleto, M. A. Cotta, S. L. Morelhão, and L. P. Cardoso, *Cryst. Growth Des.* **10**, 3436 (2010).
- <sup>9</sup>R. Lang, A. S. de Menezes, A. O. dos Santos, S. Reboh, E. A. Meneses, L. Amaral, and L. P. Cardoso, *J. Appl. Cryst.* **46**, 1796 (2013).
- <sup>10</sup>M. Renninger, *Z. Phys. A Hadrons Nucl.* **106**, 141 (1937).
- <sup>11</sup>S. L. Morelhão and L. P. Cardoso, *J. Appl. Cryst.* **29**, 446 (1996).
- <sup>12</sup>I. R. Entin, *Phys. Status Solidi A* **106**, 25 (1988).
- <sup>13</sup>V. I. Khrupa, V. V. Nikolaev, and M. YA. Skorokhod, *Phys. Stat. Solidi* **116**, K141 (1989).
- <sup>14</sup>J. F. Ziegler, J. P. Biersack, and U. Littmark, *The Stopping and Range of Ions in Solids* (Pergamon, New York, 1985).
- <sup>15</sup>K. Wittmaack, *Nucl. Instrum. Methods Phys. Res. B* **267**, 2846 (2009).
- <sup>16</sup>Hj. Matzke, *Radiat. Eff.* **3**, 93 (1970).
- <sup>17</sup>K. S. Jones and G. A. Rozgonyi, in *Rapid Thermal Processing: Science and Technology*, edited by R. B. Fair (Academic Press, Inc., San Diego, 1993), Chap. 5.
- <sup>18</sup>C. A. Cima, H. Boudinov, J. P. de Souza, Y. Suprun-Belovich, and P. F. P. Fichtner, *J. Appl. Phys.* **88**, 1771 (2000).
- <sup>19</sup>C. Bonafos, D. Mathiot, and A. Claverie, *J. Appl. Phys.* **83**, 3008 (1998).
- <sup>20</sup>W. H. Zachariasen, *Acta Cryst.* **18**, 705 (1965).
- <sup>21</sup>J. Als-Nielsen and D. McMorrow, *Elements of Modern X-Ray Physics* (John Wiley & Sons Ltd., West Sussex, 2001).
- <sup>22</sup>R. O. Freitas, A. A. Quivy, and S. L. Morelhão, *J. Appl. Phys.* **105**, 036104 (2009).
- <sup>23</sup>A. Authier, *Dynamical Theory of X-Ray Diffraction* (Oxford University Press Inc., New York, 2001).